UC Berkeley
UC Berkeley Previously Published Works

Title
Erratum: “PAPER-64 Constraints on Reionization: The 21 cm Power Spectrum at z = 8.4” (2015, ApJ, 809, 61)

Permalink
https://escholarship.org/uc/item/036231r7

Journal
The Astrophysical Journal, 863(2)

ISSN
0004-637X

Authors
Ali, Zaki S
Parsons, Aaron R
Zheng, Haoxuan
et al.

Publication Date
2018-08-20

DOI
10.3847/1538-4357/aad7b4

Peer reviewed

eScholarship.org Powered by the California Digital Library
University of California

Visualization of Colloidal Nanocrystal Formation and Electrode-Electrolyte Interfaces in Liquids Using TEM

Zhiyuan Zeng,[1] Wenjing Zheng,[1,2] and Haimei Zheng[1,3*]

[1]*Materials Sciences Division, Lawrence Berkeley National Laboratory, Berkeley, CA 94720, USA*
[2]*Department of Materials Science and Engineering, Tianjin University, Tianjin* 300350, China
China
[3]*Department of Materials Science and Engineering, University of California, Berkeley, CA 94720, USA*

[*]Correspondence to: hmzheng@lbl.gov

Conspectus

Transmission electron microscopy (TEM) has become a powerful analytic tool for addressing unique scientific problems in chemical sciences as well as in materials sciences and other disciplines. There has been a lot of recent interest in the development and applications of liquid environmental cell TEM. In this paper, we review the development and applications of Liquid cell TEM for the study of dynamic phenomena at liquid-solid interfaces focusing on two areas: (1) nucleation, growth and self-assembly of colloidal nanocrystals and (2) liquid electrode-electrolyte interfaces during charge and discharge processes. We highlight the achievements and progress that have been made in these two topical areas of our studies. For example, tracking single platinum particle growth trajectories revealed that two different pathways of growth either by monomer attachment or coalescence between nanoparticles led to the same particle size. With the improved spatial resolution and fast electron detection, we were able to trace individual facet development during platinum nanocube formation. The results show that different from the surface energy minimization rule prediction, the growth rates of all low energy facets, such as {100}, {110} and {111}, were similar. The {100} facets stopped growth early, thus the continuous growth of the rest facets resulted in a nanocube. Density Functional Theory (DFT) calculation shows that the amine ligands with low mobility on the {100} facets blocked the further growth of the facets. The ligand effects on nanoparticle shape evolution were further studied systematically using a Pt-Fe nanoparticle system by changing the oleylamine concentration. With 20%, 30% or 50% oleylamine, Pt-Fe nanowires or nanoparticles with different morphology and stability were achieved. Real time imaging of nanoparticles in solution also enabled the study of interactions between nanoparticles during self-assembly. We further compared the study

of noble metal nanoparticles and transition metal oxides in a liquid cell to elucidate the nanoparticle formation mechanisms. In the second part of this paper, we review the study of electrolyte-electrode interfaces by the development of electrochemical liquid cell TEM. The formation of single crystalline Pb dendrites from polycrystalline branches and Li dendrites growth in a commercial electrolyte for Li ion batteries were observed. We also studied lithiation reactions of MoS_2 and Au electrodes. MoS_2 nanoflakes on the Ti electrode underwent irreversible decomposition resulting in the vanishing of the MoS_2 active nanoflakes. More detailed study using nanobeam diffraction indicated that MoS_2 nanoflakes broken down into small nanoparticles due to the fast discharge. For the lithiation of Au electrodes, three distinct types of morphology changes during reactions, including gradual dissolution, explosive reaction and local expansion/shrinkage, were revealed. Additionally, we studied electrolyte decomposition reactions such as bubble formation and solid electrolyte interface (SEI) formation. At the end, our perspective on the challenges and opportunities in the applications of liquid environmental cell TEM for the study of liquid chemical reactions is provided.

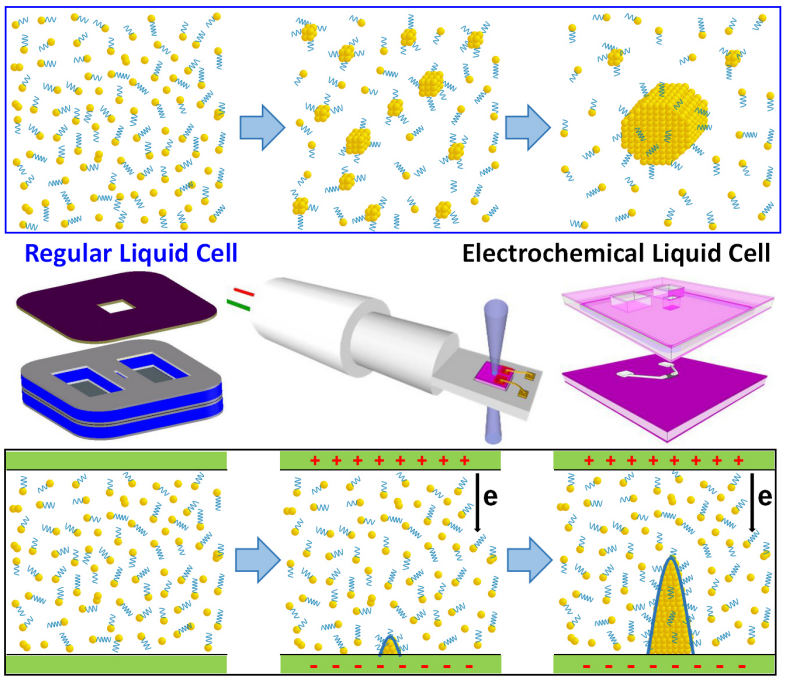

1. Introduction

Transmission electron microscopy (TEM) has been extensively used in high resolution characterization of materials in materials science, physics and chemistry. TEM has also been an indispensable tool in imaging of fine biological structures at cryogenic temperature[1]. In recent years, it has become more and more popular in using TEM to study chemical reactions in liquids[2-4] or gases[5] in situ; significant advances have been made in liquid environmental electron microscopy development and applications.[3,6,7] In this article, we review progresses in imaging through liquids with TEM highlighting

some work of our group in the past a few years on TEM visualization of colloidal nanocrystal growth and electrochemical liquid reactions (**Figure 1**).

The study of liquid phase reactions and an understanding of solid-liquid interfaces are significant for various applications ranging from solution based synthesis to energy conversion and fuel generation, catalysis, materials corrosion protection and water separation. To develop an understanding and ultimately controlling of the dynamic processes at solid-liquid interfaces often requires the atomic or molecular level study of liquid reactions in situ. Characterization of liquid samples using TEM is challenging because of the incompatibility with the high vacuum environment needed for electron microscopy. Hence, the development of liquid cells allowing for imaging through liquids with TEM has attracted lots of attention in recent years. With nanofabricated liquid cells using revolutionary thin SiN_x window cells and integrated electrodes, it has enabled to address many scientific problems concerning solid-liquid interfaces with high spatial and temporal resolution that are previously impossible. Recent applications of liquid environmental cell electron microscopy include the study of solution phase nanoparticle growth and assembly, electrochemical deposition, lithiation of electrode materials in batteries, tracing or manipulating nanoparticles, catalysis, imaging of biological materials in liquid water and so on.[1,8-11]

2. Nucleation & Growth of Colloidal Nanocrystals

2.1 Growth pathways

An understanding of colloidal nanocrystal growth mechanisms is significant for the syntheses of nanocrystals with desired physical and chemical properties. Many growth models for achieving monodisperse nanocrystals are built upon nucleation followed by growth via monomer attachment[12]. However, there have been numerous reports showing that monodisperse nanocrystals can be achieved by nanoparticle coalescence, where different nanoparticles agglomerate together to form a bigger nanoparticle,[13-15] or via oriented attachment[1], where nanoparticles attached together with the aligned crystal orientation to form a larger single crystal. This is contradictory intuitively, assuming that growth via particle coalescence or agglomeration is uncontrollably fast resulting in polydispersity, thus particle coalescence should be avoided. The ability to observe single nanoparticle growth trajectories provides the opportunity to elucidate nanocrystal growth mechanisms, where TEM liquid cells are the key development allowing to image through liquids with nanometer or atomic resolution in real time while reactions proceed.

Zheng et al. developed ultra-thin self-contained liquid cells and first applied them to study colloidal platinum nanocrystals by solution chemistry using TEM[2]. As shown in **Figure 2,** observations revealed that monodisperse nanocrystals can be achieved by nanoparticles growing simultaneously via different pathways: atomic attachment and particle coalescence. Real time imaging further indicates that particles formed by simple

monomer attachment show continuous increase of particle size with single crystalline characteristics throughout the growth. The coalesced particle is polycrystalline at the beginning. It subsequently undergoes shape changes and finally forms a single crystalline particle. During such a restructuring process, the growth by monomer attachment slows down. Thus, two different growth pathways lead to the same particle size. (**Figure 2E**). Through the combination of these two routes, an initially broad size distribution can spontaneously narrow down into a nearly monodisperse distribution. There are important questions concerning the nanoparticle growth by coalescence. For example, how do nanoparticles interact with each other? What are the forces between nanoparticles? The answers to these questions are important to nanoparticle synthesis as well as the self-assembly of nanoparticles into thin films or large three dimensional structures. Previous studies show that colloidal nanocrystals take different pathways of growth driven by their size- and morphology-dependent internal energy and details has been reported in previous publications.[2,16,17]

2.2 Nanoparticle shape evolution

Liquid environmental cell electron microscopy has been used to reveal the shape evolution of nanoparticles, where formation mechanisms of nanocubes, nanorods, plates, etc. can be resolved. A liquid cell with a small amount of liquid can be encapsulated inside a high-vacuum microscope for an extended period of time. It allows nanoparticles to nucleate and fully develop into different shape. Nanocrystal nucleation and growth can be initiated by thermal heating[18] or, more commonly, by electron beam irradiation[9]. Despite many unknown factors in electron beam activated reactions, nanocrystals similar to those in flask synthesis have been achieved in a liquid cell.[19,20,21]

Zheng group reported TEM imaging of platinum nanocube growth in a liquid cell with high spatial and temporal resolution[21] (**Figure 3A-B**). Tracking of individual facet evolution shows that growth rates of all low index facets, e.g., {100}, {110} and {111}, are similar until the {100} facets stop growth. The continuous growth of the rest facets leads to a nanocube. Calculation indicates that the arresting of {100} growing facets can be attributed to the lower ligand mobility on the {100} facets. At the end, only the {111} facets grow filling the corners until the nanoparticle becomes a cube. This study provided critical insights on the role of ligands in controlling of nanocrystal shape evolution. It was also concluded that at the nanoscale stochastic nature dominants the nanocrystal growth, which is different from the Wulff construction prediction that the higher-energy facets grow faster and the nanocrystal morphology is determined by the relative surface energies of the different crystalline facets.[12,22]

Many recent studies show that nanoparticles act as “artificial atoms” to serve as the basic building blocks for the synthesis of hierarchical nanostructures.[12,22] As it was discussed in the previous session small nanoparticles interact with each other to form a large single crystal through oriented attachment.[23,24] Liao et al. reported the solution

growth of Pt_3Fe nanorods, where a nanoparticle chain was achieved by shape-directed nanoparticle attachment and the subsequent straightening of the chain with crystal orientation correction resulted in a single-crystal nanorod. Tracking the nanoparticle growth trajectories assisted to differentiate the forces exerted by a single nanoparticle or a nanoparticle chain (**Figure 3C-D**).[16]

A systematic study of ligands effects on nanoparticle formation was further carried out (**Figure 3E-F**).[25] By changing the oleylamine concentration from 30% to 20%, nanoparticles were end-to-end attached together to form a nanowire. The nanowire subsequently broke down into pieces and each piece shrank into a round particle. A large size distribution of the nanoparticles was observed. With a higher concentration of oleylamine, such as 50% or more, the individual nanoparticles were stable in solution.

Interaction between nanoparticles can be complex, where a variety of forces may be involved for instance, van der Waal forces, electric or magnetic dipolar forces, liquid surface tension in dying mediated self-assembly, etc.[24,26,27] Powers et al. observed and quantified the complex dynamics of Pt-Fe nanoparticle self-assembly directly.[17] The long-range anisotropic electric dipolar forces and the close-range van der Waal interactions result in formation of loosely packed clumps.[17] The chains either fold to form locally packed clumps or a two-dimensional film (**Figure 4A**). The results prove that the long-range forces and particle interactions observed for $PtFe_3$ are inherent to particle properties (**Figure 4B**). As another example, nanoparticles can form at the oil-water interface with oil droplets distributed within the water phases. The phenomenon is named for the characteristic ring-like deposit along the perimeter of oil liquid droplet[28]. The mechanism behind the formation of these and similar rings is known as the coffee ring effect **(Figure 4D).**

2.3 Metal vs oxide nanoparticle growth

Transition metal oxides, for instance, spinel ferrites MFe_2O_4 with M (II) corresponding to Fe^{2+}, Mn^{2+}, Ni^{2+}, Zn^{2+}, or Cu^{2+}, have a broad of applications ranging from biomedicine[29] to catalysis,[30] and high-density magnetic storage.[31] An understanding of their formation mechanisms and ultimately controlling of the synthesis have been of great interest. There have been many studies on in situ observation of noble metal nanocrystal formation using liquid cell TEM to elucidate the electron beam-induced growth mechanisms.[32,33] However, there are limited reports on the formation of metal oxide nanoparticles in a liquid cell.

Liang et al. reported the study of M-Fe-oxide (M = Ni, Mn, Co, or Zn) nanoparticles using liquid cell TEM.[34,35] A growth solution of metal acetylacetonates dissolved in oleylamine, oleic acid, and benzyl ether was used. Nickel iron oxide or cobalt iron oxide nanocrystals with spinel structure were obtained under electron beam irradiation of the Ni-Fe or Co-Fe precursor solution (**Figure 5A**). The study also showed that with the solution containing Mn-Fe or Zn-Fe precursor, iron oxide nanoparticles were achieved

with Mn or Zn remaining in the solution (**Figure 5B**). It was found that ternary oxides (i.e., Ni-Fe-oxide and Co-Fe-oxide) were achieved when the two precursors have the smaller ΔEr and ΔTd, such as Ni-Fe and Co-Fe mixed precursor solution; while single metal component oxide with lower Td and stronger Er (i.e., Fe-oxide) was obtained, for example, Mn-Fe or Zn-Fe mixed precursor solution.[34] These results shed light on synthetic strategies for incorporating multiple components in the oxide nanostructures.

Further study using a Fe-Pt precursor solution, Liang et al. obtained metal-transition oxide core-shell nanostructures[35] (**Figure 5**). Based on the detailed characterization using X-ray energy dispersive spectroscopy (EDS) elemental mapping, electron energy loss spectroscopy (EELS), and high resolution structure analysis, Fe_3Pt-Fe_2O_3 core-shell structure was confirmed. The formation mechanism of Fe_3Pt-Fe_2O_3 core-shell nanoparticles was proposed, as shown in **Figure 5E**. Briefly, Pt ions are reduced to metal under the electron beam due to the higher redox potential as well as the lower decomposition temperature of $Pt(acac)_2$ compared to $Fe(acac)_3$.[36] Once Pt^0 is formed, oleylamine ligands ($R\text{-}NH_2$) prefer to bind with Pt (Stage I).[37] Thus, Fe^{3+} ions can be reduced to form Fe_3Pt, where Pt catalyzes the electron transfer between oleylamine and Fe ions.[36] When Pt is depleted in the precursor solution, the nanoparticle core size is fixed and the absorbed Fe ions on the nanoparticle surface develop into iron oxide without further reduction. Most nanoparticles show polycrystalline shell, likely due to the large lattice mismatch between Fe_3Pt and α-Fe_2O_3.[35]

It is noted that besides nanoparticle growth, etching of nanoparticles has also been observed in liquid cells[38,39] Schneider et al. and others[39-42] showed that electron beam plays an important role in crystallization as well as etching. Thus, quantitative study of the electron beam effects is necessary to elucidating growth mechanisms observed in a liquid cell under TEM.

3. Crystallization & Reactions under Electrochemical Bias

3.1 Dendritic growth

Dendritic growth has attracted lots of research interest in recent years[43-47]. It is ubiquitous in materials solidification and crystallization, which arises from the instabilities when growth rate is limited by the diffusion of ions from solution to the deposits. Dendrites formation can induce device failure, for example, a dendrite may connect two electrodes of a battery cell. Real time observation of the electrochemical growth with high spatial resolution provides the opportunity to elucidate the dendrite growth mechanisms and insights on new strategies of reducing battery failure. [7,8,48,49]

Sun et al. reported in situ TEM imaging of the deposition and dissolution of lead dendrites on the electrodes during discharge-charge processes.[50] Unique crystallization pathways were revealed. As shown in **Figure 6A and B**, Pb ions were first reduced to form small grains on the electrode. Subsequently, those grains were aggregated to form a

large cluster with polycrystalline features. Eventually, a single crystalline structure is achieved through the interactions between nanograins and recrystallization.

Using a commercial electrolyte for lithium ion batteries, we have also observed lithium dendrite growth in situ. As shown in **Figure 6C**, the lithium dendrite nucleates between two bubbles and grow rapidly on the Au alloy layer (highlighted by blue arrows). The lithium dendrite preserves the shape for a short time; when the voltage is swept back the localized Li stripping occurs thus the dendrite is dissolved eventually.

There are other reports on in situ observation of electrodeposition related to dendrite formation. For example, Radisic et al.[48] reported imaging of electrochemical deposition of polycrystalline Au using an electrochemical liquid cell. Chen et al.[51] achieved deposition of nickel nanograins with a homemade TEM cell. White et al.[52] captured electrodeposition and stripping of lead on polycrystalline gold electrodes.

3.2 Electrode reactions: MoS_2 dissolution and Au lithiation reaction

Recently, we have observed lithiation/delithiation of MoS_2 nanosheets in a $LiPF_6$/EC/DEC commercial electrolyte.[53] There have been a series of related studies on lithiation and delithiation induced structural transformation using in situ TEM.[53-56] For instance, the lithiation and delithiation of Si nanowire electrodes during electrochemical testing[54] showed that the first lithiation of Si nanoparticle leads to anisotropic volume expansion favoring the ⟨110⟩ directions followed by isotropic expansion.[57] There has also been studies on atomic imaging of lithium insertion and extraction dynamics in partially delithiated $LiFePO_4$[58] and random solid solution zone in $LiFePO_4$ electrode[59]; the breakdown of a range of inorganic/salt complexes in Li-ion batteries.[56]

Our observation of lithiation/delithiation of MoS_2 nanosheets showed that MoS_2 on the Ti electrode underwent irreversible decomposition resulting in fast dissolution and vanishing of MoS_2 nanoflakes (**Figure 7A**), which is consistent with other literature reports on electrode materials dissolution and the lithium polysulfide shuttling effects in a real battery cell.[60] Repeated experiments also indicate lithiation induced structural expansion and deformation of MoS_2 nanosheets, In addition, fast discharge induces "explosion" of some MoS_2 nanosheets into 5-10 nm MoS_2 nanoparticles (details see previous publications[4,53]).

It has been a serious issue that mechanical stress can be generated during lithiation and delithiation processes, which induces pulverization with rapid capacity fading. Although different Au-Li alloy phases have been identified through both ex situ and in situ studies,[61-64] the Au-Li reaction has never been observed directly. We studied the lithiation of Au electrode in an electrochemical liquid cell by using commercial liquid electrolyte for lithium ion batteries.[65] Three distinct types of morphology changes were observed during the reaction, including gradual dissolution, explosive reaction and local expansion/shrinkage. The local expansion/shrinkage of the Au electrode during lithiation induces cracks was likely due to the inhomogeneous lithiation reactions (**Figure 7C**). The

explosive Li-Au reaction was attributed to the gaseous products being absorbed and accumulated on the electrode surface, which trigger the explosion of Au electrode at a later stage (**Figure 7D**). As to the gradual dissolution, the Au electrode could react intensively with the electrolyte resulting in the stripping and dissolving of Au from the outer layer into the inner layer of the electrode, as shown in **Figure 7E**.

3.3 Electrolyte decomposition: solid electrolyte interphase (SEI) and bubble formation

In general, the electrolyte solutions for Li batteries are comprised of redox couples, with the solvent as a reductant and the salt as an oxidant. The majority of species that are oxidized are the solvent molecules, not the salt anions[66,67] The breakdown of a range of inorganic/salt complexes and reactions between complexes lead to formation of solid-electrolyte interphase (SEI).[68,69] SEI layer protects the electrolytic solution and other battery components from undesirable reduction or oxidation. However, gas production during SEI formation on the active electrode can introduce defects and strain in the SEI film thus peeling of SEI from the electrode.[49,53] There have been limited in situ studies on direct observation and characterization of SEI, largely due to SEI is air sensitive and it is hard to analyze it in a battery cell.

Zeng et al. achieved real time observation of SEI formation using electrochemical liquid cell TEM.[49,65] As shown in **Figure 8A**, SEI film grows on the electrode due to the reduction of electrolyte corresponding to the electric sweeping (4 to 0 V) on the other electrode. At the beginning, a thin SEI layer was observed on the Au electrode. Subsequently, a gap between the SEI film and the electrode was observed, the emerged void expands promptly between the SEI layer and active electrode, likely due to the released gas accompanied by the reactions of active electrode materials. EDS analysis of SEI shows the presence of C, O, and F elements and their distributions. Further 4D STEM analysis of SEI indicates LiF nanocrystals (4-5 nm) distributed within the whole amorphous matrix layer (details see the previous publication[53]). Since it is hard to detect the amorphous or small crystalline components by nanobeam diffraction, it cannot exclude the presence of other inorganic components (e.g., Li_2CO_3, Li_2O) within the SEI. Note that the gaseous products have been observed in many other electrochemical experiments. For example, **Figure 8B** shows bubble formation, likely PF_5 from electrolyte decomposition. A large bubble is obtained by the accumulation and merging of many tiny bubbles (**Figure 8C**). By replacement of Au with Ti electrode, bubble formation can be significantly reduced, which suggests Au may catalyze the bubble generation.[65]

4. Electron Beam Effects

The high-energy electron beam effects on solid samples have been studied both theoretically and experimentally.[70] However, the electron beam effects during imaging liquid samples can be different from the solids, depending on the specific systems and the role of various factors, such as solvated electrons, bond cleavage, and local heating,

which make the radiation damage mechanisms more complicated and system dependent.[7] When liquid cell TEM is used to study nanoparticle growth, the electron beam is often an energy source to trigger the reaction. The high-energy electron beam can induce the decomposition of liquid or precursor. Nanoparticle growth under the electron beam occurs above a certain dose threshold. However, with a sufficiently high dose rate, gaseous products, such as bubbles, can be generated in an aqueous solution, given that various radicals, including secondary electrons, can be generated and these species can further participate in the reactions.[71] To minimize the electron beam damage, one can consider reducing the accelerating voltage or lowering the electron dose. As all electron beam effects are dose dependent, low-dose imaging can be an effective way to reduce electron beam damage in all systems. For electrochemical deposition using liquid cell TEM, beam effects are minimized at the reduced electron dose during imaging.[48,72,73] The observed dendritic growth or electrolyte decomposition were achieved only when an electric bias was applied in the electrochemical cell.[49,50,53]

Future Perspectives

The ability to image through liquids with TEM has opened tremendous opportunities to study liquid phase reactions and to reveal dynamic phenomena at solid-liquid interfaces in situ with high spatial and temporal resolution. In addition to visualizing the colloidal nanocrystal growth and assembly and liquid phase electrochemical reactions as discussed in this article, there are many other applications of liquid environmental cell electron microscopy, such as, imaging of soft or biological materials in liquid water, materials corrosion or catalysis. Future advances in atomic resolution liquid cell TEM would enable a significant leap in the study of materials dynamic processes *in situ*.

A new liquid cell platform (**Figure 9**) is needed to achieve fast, atomic resolution TEM imaging through liquids beyond the limits of current imaging capabilities. Such a platform is built upon new liquid cell development, advanced imaging, fast electron detection, computational design and data analysis. With such a platform allowing the controlled reactions in a liquid cell, advanced image acquisition with atomic resolution and at a fast speed, integrated analytical capabilities, comprehensive data processing and interpretation, our study of chemical reactions in solution will be revolutionized.

For the study of liquid phase reactions or materials dynamic phenomena at liquid-solid interfaces, we may also fully take advantages of the aberration corrected electron microscope, advanced detector and other instrumentation development. As we know that TEM has advanced significantly with the aberration corrected optics, imaging with 0.5 Å spatial resolution[74] and electron energy loss spectroscopy (EELS) with 1 or 2 meV energy resolution[75] have been achieved. With the combination of revolutionary EDS development, TEM is becoming more and more powerful in characterization of atomic structure, bonding, chemical and structural related properties of materials. In addition, with the development of advanced detector,[21] high speed data acquisition with 2.5 milliseconds temporal resolution[21] has also been obtained. Additionally, other factors, such as, optimizing sample thickness, limiting electron beam damage, control of sample environment especially the liquid reaction or mixing, and quantitative measurements of reaction products are also critical to revealing of dynamic phenomena at liquid-solid

interfaces with high resolution. These efforts promote TEM as an analytical tool for chemical sciences in addition to materials science, physics and biology.

Supporting Information

Supporting movies corresponding to some of the figures were provided. This material is available free of charge via the Internet at http://pubs.acs.org.

Acknowledgments

We acknowledge the support of the U.S. Department of Energy, Office of Science, Office of Basic Energy Sciences, Materials Sciences and Engineering Division under Contract No. DE-AC02-05-CH11231 within the KC22ZH program.

Biographical Information

Zhiyuan Zeng obtained his BE in Materials Physics from the Central South University, China (2006), and his ME from the Department of Materials Science and Engineering, Zhejiang University, China (2008). He completed his PhD in the School of Materials Science and Engineering of Nanyang Technological University, Singapore (2013). From February 2013, he started the Physicist Postdoc Fellow in Materials Sciences Division at Lawrence Berkeley National Laboratory under Dr. Haimei Zheng. His current research focuses on in situ multimodal characterization of Li/Na batteries and two-dimensional nanosheets applications.

Wenjing Zheng obtained her B.S. in Chemical Engineering and Technology from Taizhou University in China (2010) and M.S. in Material Engineering from Shijiazhuang Tiedao University in China (2014). She is currently a Ph.D. Candidate of Tianjin University and a visiting student in Lawrence Berkeley National Laboratory. She is interested in nanoscale materials design, mechanisms and catalysts.

Haimei Zheng earned her Ph.D with Prof. Ramamoorthy Ramesh and Prof. Lourdes Salamanca-Riba at University of Maryland, College Park (2004). She was a postdoc with Prof. Paul Alivisatos in Department of Chemistry at University of California, Berkeley and jointly at National Center for Electron Microscopy of Lawrence Berkeley National Laboratory. Currently, she is a senior staff scientist in Materials Sciences Division at Lawrence Berkeley National Laboratory and an adjunct professor in Department of Materials Science and Engineering at University of California, Berkeley. The primary research in her group is on physical and chemical processes of materials with a focus on liquid-solid interfaces including nucleation, growth, self-assembly of nanoparticles and electrolyte-electrode interfaces during electrochemical processes.

References

(1) Mirsaidov, U. M.; Zheng, H. M.; Casana, Y.; Matsudaira, P. Imaging protein structure in water at 2.7 nm resolution by transmission electron microscopy. *Biophys. J.* **2012**, *102*, L15-L17.

(2) Zheng, H.; Smith, R. K.; Jun, Y.-w.; Kisielowski, C.; Dahmen, U.; Alivisatos, A. P. Observation of single colloidal platinum nanocrystal growth trajectories. *Science* **2009**, *324*, 1309-1312.

(3) Ross, F. M. Opportunities and challenges in liquid cell electron microscopy. *Science* **2015**, *350*, aaa9886.

(4) Liao, H. G.; Zheng, H. M. Liquid cell transmission electron microscopy. Annu. Rev. Phys. Chem. 2016, 67, 719-747.

(5) Yoshida, H.; Kuwauchi, Y.; Jinschek, J. R.; Sun, K. J.; Tanaka, S.; Kohyama, M.; Shimada, S.; Haruta, M.; Takeda, S. Visualizing gas molecules interacting with supported nanoparticulate catalysts at reaction conditions. *Science* **2012**, *335*, 317-319.

(6) Zheng, H. M.; Meng, Y. S.; Zhu, Y. M. Frontiers of in situ electron microscopy. *MRS Bull.* **2015**, *40*, 12-18.

(7) de Jonge, N.; Ross, F. M. Electron microscopy of specimens in liquid. *Nat. Nanotechnol.* **2011**, *6*, 695-704.

(8) Williamson, M. J.; Tromp, R. M.; Vereecken, P. M.; Hull, R.; Ross, F. M. Dynamic microscopy of nanoscale cluster growth at the solid-liquid interface. *Nat. Mater.* **2003**, *2*, 532-536.

(9) Gai, P. L. Developments in in situ environmental cell high-resolution electron microscopy and applications to catalysis. *Top. Catal.* **2002**, *21*, 161-173.

(10) Liu, K.-L.; Wu, C.-C.; Huang, Y.-J.; Peng, H.-L.; Chang, H.-Y.; Chang, P.; Hsu, L.; Yew, T.-R. Novel microchip for in situ TEM imaging of living organisms and bio-reactions in aqueous conditions. *Lab Chip* **2008**, *8*, 1915-1921.

(11) Jonge, N. d.; Peckys, D. B.; Kremers, G. J.; Piston, D. W. Electron microscopy of whole cells in liquid with nanometer resolution. *Proc. Natl. Acad. Sci. USA* **2009**, *106*, 2159-2164.

(12) Yin, Y.; Alivisatos, A. P. Colloidal nanocrystal synthesis and the organic-inorganic interface. *Nature* **2005**, *437*, 664-670.

(13) Banfield, J. F.; Welch, S. A.; Zhang, H.; Ebert, T. T.; Penn, R. L. Aggregation-based crystal growth and microstructure development in natural iron oxyhydroxide biomineralization products. *Science* **2000**, *289*, 751-754.

(14) Pacholski, C.; Kornowski, A.; Weller, H. Self-assembly of ZnO: from nanodots to nanorods. *Angew. Chem. Int. Ed.* **2002**, *41*, 1188-1191.

(15) Watzky, M. A.; Finney, E. E.; Finke, R. G. Transition-metal nanocluster size vs formation time and the catalytically effective nucleus number: a mechanism-based treatment. *J. Am. Chem. Soc.* **2008**, *130*, 11959-11969.

(16) Liao, H.-G.; Cui, L.; Whitelam, S.; Zheng, H. Real-time imaging of Pt_3Fe nanorod growth in solution. *Science* **2012**, *336*, 1011-1014.

(17) Powers, A. S.; Liao, H.-G.; Raja, S. N.; Bronstein, N. D.; Alivisatos, A. P.; Zheng, H. Tracking nanoparticle diffusion and interaction during self-assembly in a liquid cell. *Nano Lett.* **2017**, *17*, 15-20.

(18) Xin, H. L. L.; Zheng, H. M. In situ observation of oscillatory growth of bismuth nanoparticles. *Nano Lett.* **2012**, *12*, 1470-1474.

(19) Yuk, J. M.; Park, J.; Ercius, P.; Kim, K.; Hellebusch, D. J.; Crommie, M. F.; Lee, J. Y.; Zettl, A.; Alivisatos, A. P. High-resolution EM of colloidal nanocrystal growth using graphene liquid cells. *Science* **2012**, *336*, 61-64.

(20) Borodko, Y.; Ercius, P.; Zherebetskyy, D.; Wang, Y.; Sun, Y.; Somorjai, G. From single atoms to nanocrystals: photoreduction of $[PtCl_6]^{2-}$ in aqueous and tetrahydrofuran solutions of PVP. *J. Phys. Chem. C* **2013**, *117*, 26667-26674.

(21) Liao, H.-G.; Zherebetskyy, D.; Xin, H.; Czarnik, C.; Ercius, P.; Elmlund, H.; Pan, M.; Wang, L.-W.; Zheng, H. Facet development during platinum nanocube growth. *Science* **2014**, *345*, 916-919.

(22) Manna, L.; Scher, E. C.; Alivisatos, A. P. Synthesis of soluble and processable rod-, arrow-, teardrop-, and tetrapod-shaped CdSe nanocrystals. *J. Am. Chem. Soc.* **2000**, *122*, 12700-12706.

(23) Schliehe, C.; Juarez, B. H.; Pelletier, M.; Jander, S.; Greshnykh, D.; Nagel, M.; Meyer, A.; Foerster, S.; Kornowski, A.; Klinke, C.; Weller, H. Ultrathin PbS sheets by two-dimensional oriented attachment. *Science* **2010**, *329*, 550-553.

(24) Cho, K.-S.; Talapin, D. V.; Gaschler, W.; Murray, C. B. Designing PbSe nanowires and nanorings through oriented attachment of nanoparticles. *J. Am. Chem. Soc.* **2005**, *127*, 7140-7147.

(25) Liao, H.-G.; Zheng, H. Liquid cell transmission electron microscopy study of platinum iron nanocrystal growth and shape evolution. *J. Am. Chem. Soc.* **2013**, *135*, 5038-5043.

(26) Min, Y.; Akbulut, M.; Kristiansen, K.; Golan, Y.; Israelachvili, J. The role of interparticle and external forces in nanoparticle assembly. *Nat. Mater.* **2008**, *7*, 527-538.

(27) Yusuf, H.; Kim, W.-G.; Lee, D. H.; Guo, Y.; Moffitt, M. G. Size control of mesoscale aqueous assemblies of quantum dots and block copolymers. *Langmuir* **2007**, *23*, 868-878.

(28) Zhou, Y.; Zhang, X.; Xu, T.; Bustillo, K.; Sun, L.; Zheng, H. Liquid droplet mediated CoO nanoparticle ring formation. *Submitted* **2017**.

(29) Kumar, C. S. S. R.; Mohammad, F. Magnetic nanomaterials for hyperthermia-based therapy and controlled drug delivery. *Adv. Drug Deliv. Rev.* **2011**, *63*, 789-808.

(30) Polshettiwar, V.; Luque, R.; Fihri, A.; Zhu, H. B.; Bouhrara, M.; Bassett, J. M. Magnetically recoverable nanocatalysts. *Chem. Rev.* **2011**, *111*, 3036-3075.

(31) Frey, N. A.; Peng, S.; Cheng, K.; Sun, S. Magnetic nanoparticles: synthesis, functionalization, and applications in bioimaging and magnetic energy storage. *Chem. Soc. Rev.* **2009**, *38*, 2532-2542.

(32) Woehl, T. J.; Jungjohann, K. L.; Evans, J. E.; Arslan, I.; Ristenpart, W. D.; Browning, N. D. Experimental procedures to mitigate electron beam induced artifacts during in situ fluid imaging of nanomaterials. *Ultramicroscopy* **2013**, *127*, 53-63.

(33) Woehl, T. J.; Evans, J. E.; Arslan, I.; Ristenpart, W. D.; Browning, N. D. Direct in situ determination of the mechanisms controlling nanoparticle nucleation and growth. *ACS Nano* **2012**, *6*, 8599-8610.

(34) Liang, W.-I.; Zhang, X.; Bustillo, K.; Chiu, C.-H.; Wu, W.-W.; Xu, J.; Chu,

Y.-H.; Zheng, H. In situ study of spinel ferrite nanocrystal growth using liquid cell transmission electron microscopy. *Chem. Mater.* **2015**, *27*, 8146-8152.

(35) Liang, W.-I.; Zhang, X.; Zan, Y.; Pan, M.; Czarnik, C.; Bustillo, K.; Xu, J.; Chu, Y.-H.; Zheng, H. In situ study of Fe_3Pt–Fe_2O_3 core–shell nanoparticle formation. *J. Am. Chem. Soc.* **2015**, *137*, 14850-14853.

(36) Beck, W.; Souza, C. G. S.; Silva, T. L.; Jafelicci, M.; Varanda, L. C. Formation mechanism via a heterocoagulation approach of FePt nanoparticles using the modified polyol process. *J. Phys. Chem. C* **2011**, *115*, 10475-10482.

(37) Shukla, N.; Liu, C.; Jones, P. M.; Weller, D. FTIR study of surfactant bonding to FePt nanoparticles. *J. Magn. Magn. Mater.* **2003**, *266*, 178-184.

(38) Ye, X. C.; Jones, M. R.; Frechette, L. B.; Chen, Q.; Powers, A. S.; Ercius, P.; Dunn, G.; Rotskoff, G. M.; Nguyen, S. C.; Adiga, V. P.; Zettl, A.; Rabani, E.; Geissler, P. L.; Alivisatos, A. P. Single-particle mapping of nonequilibrium nanocrystal transformations. *Science* **2016**, *354*, 874-877.

(39) Schneider, N. M.; Norton, M. M.; Mendel, B. J.; Grogan, J. M.; Ross, F. M.; Bau, H. H. Electron-water interactions and implications for liquid cell electron microscopy. *J. Phys. Chem. C* **2014**, *118*, 22373-22382.

(40) Ahn, T. Y.; Hong, S. P.; Kim, S. I.; Kim, Y. W. In situ liquid-cell transmission electron microscopy for direct observation of concentration-dependent growth and dissolution of silver nanoparticles. *Rsc Adv.* **2015**, *5*, 82342-82345.

(41) Jiang, Y. Y.; Zhu, G. M.; Dong, G. X.; Lin, F.; Zhang, H.; Yuan, J.; Zhang, Z.; Jin, C. H. Probing the oxidative etching induced dissolution of palladium nanocrystals in solution by liquid cell transmission electron microscopy. *Micron* **2017**, *97*, 22-28.

(42) Jiang, Y. Y.; Zhu, G. M.; Lin, F.; Zhang, H.; Jin, C. H.; Yuan, J.; Yang, D. R.; Zhang, Z. In situ study of oxidative etching of palladium nanocrystals by liquid cell electron microscopy. *Nano Lett.* **2014**, *14*, 3761-3765.

(43) Tiller, W. A. Dendrites - Understanding of this familiar phenomenon has led to the development of useful man-made materials. *Science* **1964**, *146*, 871-879.

(44) Langer, J. S. Dendrites, viscous fingers, and the theory of pattern formation. *Science* **1989**, *243*, 1150-1156.

(45) Miyata, Y.; Glicksman, M. E.; Tirmizi, S. H. Dendritic growth with interfacial energy anisotropy. *J. Cryst. Growth* **1991**, *110*, 683-691.

(46) Libbrecht, K. G.; Tanusheva, V. M. Electrically induced morphological instabilities in free dendrite growth. *Phy. Rev. Lett.* **1998**, *81*, 176-179.

(47) Börzsönyi, T.; Tóth-Katona, T.; Buka, Á.; Gránásy, L. Dendrites regularized by spatially homogeneous time-periodic forcing. *Phy. Rev. Lett.* **1999**, *83*, 2853-2856.

(48) Radisic, A.; Vereecken, P. M.; Hannon, J. B.; Searson, P. C.; Ross, F. M. Quantifying electrochemical nucleation and growth of nanoscale clusters using real-time kinetic data. *Nano Lett.* **2006**, *6*, 238-242.

(49) Zeng, Z. Y.; Liang, W. I.; Liao, H. G.; Xin, H. L. L.; Chu, Y. H.; Zheng, H. M. Visualization of electrode-electrolyte interfaces in $LiPF_6$/EC/DEC electrolyte for lithium ion batteries via in Situ TEM. *Nano Lett.* **2014**, *14*, 1745-1750.

(50) Sun, M.; Liao, H.-G.; Niu, K.; Zheng, H. Structural and morphological evolution of lead dendrites during electrochemical migration. *Sci. Rep.* **2013**, *3*, 3227.

(51) Chen, X.; Noh, K. W.; Wen, J. G.; Dillon, S. J. In situ electrochemical wet

cell transmission electron microscopy characterization of solid-liquid interactions between Ni and aqueous $NiCl_2$. *Acta Mater.* **2012**, *60*, 192-198.

(52) White, E. R.; Singer, S. B.; Augustyn, V.; Hubbard, W. A.; Mecklenburg, M.; Dunn, B.; Regan, B. C. In situ transmission electron microscopy of lead dendrites and lead ions in aqueous solution. *ACS Nano* **2012**, *6*, 6308-6317.

(53) Zeng, Z.; Zhang, X.; Bustillo, K.; Niu, K.; Gammer, C.; Xu, J.; Zheng, H. In situ study of lithiation and delithiation of MoS_2 nanosheets using electrochemical liquid cell transmission electron microscopy. *Nano Lett.* **2015**, *15*, 5214-5220.

(54) Gu, M.; Parent, L. R.; Mehdi, B. L.; Unocic, R. R.; McDowell, M. T.; Sacci, R. L.; Xu, W.; Connell, J. G.; Xu, P.; Abellan, P.; Chen, X.; Zhang, Y.; Perea, D. E.; Evans, J. E.; Lauhon, L. J.; Zhang, J.-G.; Liu, J.; Browning, N. D.; Cui, Y.; Arslan, I.; Wang, C.-M. Demonstration of an electrochemical liquid cell for operando transmission electron microscopy observation of the lithiation/delithiation behavior of Si nanowire battery anodes. *Nano Lett.* **2013**, *13*, 6106-6112.

(55) Holtz, M. E.; Yu, Y.; Gunceler, D.; Gao, J.; Sundararaman, R.; Schwarz, K. A.; Arias, T. A.; Abruña, H. D.; Muller, D. A. Nanoscale imaging of lithium ion distribution during in situ operation of battery electrode and electrolyte. *Nano Lett.* **2014**, *14*, 1453-1459.

(56) Abellan, P.; Mehdi, B. L.; Parent, L. R.; Gu, M.; Park, C.; Xu, W.; Zhang, Y.; Arslan, I.; Zhang, J.-G.; Wang, C.-M.; Evans, J. E.; Browning, N. D. Probing the degradation mechanisms in electrolyte solutions for Li-ion batteries by in situ transmission electron microscopy. *Nano Lett.* **2014**, *14*, 1293-1299.

(57) Yuk, J. M.; Seo, H. K.; Choi, J. W.; Lee, J. Y. Anisotropic lithiation onset in silicon nanoparticle anode revealed by in situ graphene liquid cell electron microscopy. *ACS Nano* **2014**, *8*, 7478-7485.

(58) Gu, L.; Zhu, C. B.; Li, H.; Yu, Y.; Li, C. L.; Tsukimoto, S.; Maier, J.; Ikuhara, Y. Direct observation of lithium staging in partially delithiated $LiFePO_4$ at atomic resolution. *J. Am. Chem. Soc.* **2011**, *133*, 4661-4663.

(59) Niu, J.; Kushima, A.; Qian, X.; Qi, L.; Xiang, K.; Chiang, Y.-M.; Li, J. In situ observation of random solid solution zone in $LiFePO_4$ electrode. *Nano Lett.* **2014**, *14*, 4005-4010.

(60) Xiao, J.; Wang, X.; Yang, X.-Q.; Xun, S.; Liu, G.; Koech, P. K.; Liu, J.; Lemmon, J. P. Electrochemically induced high capacity displacement reaction of PEO/MoS_2/Graphene nanocomposites with lithium. *Adv. Funct. Mater.* **2011**, *21*, 2840-2846.

(61) Lee, Y. J.; Lee, Y.; Oh, D.; Chen, T.; Ceder, G.; Belcher, A. M. Biologically activated noble metal alloys at the nanoscale: For lithium ion battery anodes. *Nano Lett.* **2010**, *10*, 2433-2440.

(62) Taillades, G.; Benjelloun, N.; Sarradin, J.; Ribes, M. Metal-based very thin film anodes for lithium ion microbatteries. *Solid State Ionics* **2002**, *152*, 119-124.

(63) Yuan, L.; Liu, H. K.; Maaroof, A.; Konstantinov, K.; Liu, J.; Cortie, M. Mesoporous gold as anode material for lithium-ion cells. *J. New Mater. Electrochem. Syst.* **2007**, *10*, 95-99.

(64) Laik, B.; Eude, L.; Pereira-Ramos, J. P.; Cojocaru, C. S.; Pribat, D.; Rouviere, E. Silicon nanowires as negative electrode for lithium-ion microbatteries. *Electrochim. Acta* **2008**, *53*, 5528-5532.

(65) Zeng, Z.; Liang, W.-I.; Chu, Y.-H.; Zheng, H. In situ TEM study of the Li-Au reaction in an electrochemical liquid cell. *Faraday Discuss.* **2014**, *176*, 95-107.

(66) Moshkovich, M.; Gofer, Y.; Aurbach, D. Investigation of the electrochemical windows of aprotic alkali metal (Li,Na,K) salt solutions. *J. Electrochem. Soc.* **2001**, *148*, E155-E167.

(67) Aurbach, D.; Talyosef, Y.; Markovsky, B.; Markevich, E.; Zinigrad, E.; Asraf, L.; Gnanaraj, J. S.; Kim, H.-J. Design of electrolyte solutions for Li and Li-ion batteries: a review. *Electrochim. Acta* **2004**, *50*, 247-254.

(68) Unocic, R. R.; Sun, X.-G.; Sacci, R. L.; Adamczyk, L. A.; Alsem, D. H.; Dai, S.; Dudney, N. J.; More, K. L. Direct visualization of solid electrolyte interphase formation in lithium-ion batteries with in situ electrochemical transmission electron microscopy. *Microsc. Microanal.* **2014**, *20*, 1029-1037.

(69) Sacci, R. L.; Dudney, N. J.; More, K. L.; Parent, L. R.; Arslan, I.; Browning, N. D.; Unocic, R. R. Direct visualization of initial SEI morphology and growth kinetics during lithium deposition by in situ electrochemical transmission electron microscopy. *Chem. Commun.* **2014**, *50*, 2104-2107.

(70) Egerton, R. F.; Li, P.; Malac, M. Radiation damage in the TEM and SEM. *Micron* **2004**, *35*, 399-409.

(70) Egerton, R. F.; Li, P.; Malac, M. Radiation damage in the TEM and SEM. *Micron* **2004**, *35*, 399-409.

(71) Grogan, J. M.; Schneider, N. M.; Ross, F. M.; Bau, H. H. Bubble and pattern formation in liquid induced by an electron beam. *Nano Lett.* **2014**, *14*, 359-364.

(72) Radisic, A.; Ross, F. M.; Searson, P. C. In situ study of the growth kinetics of individual island electrodeposition of copper. *J. Phys. Chem. B* **2006**, *110*, 7862-7868.

(73) den Heijer, M.; Shao, I.; Radisic, A.; Reuter, M. C.; Ross, F. M. Patterned electrochemical deposition of copper using an electron beam. *APL Mater.* **2014**, *2*, 022101.

(74) Rossell, M.; Watanabe, M.; Erni, R.; Radmilovic, V.; Dahmen, U. Quantitative Li mapping in Al alloys by sub-eV resolution energy-filtering transmission electron microscopy (EFTEM) in the aberration-corrected, monochromated TEAM 0.5 instrument. *Microsc. Microanal.* **2009**, *15*, 430-431.

(75) Michel, E.; Ibach, H.; Schneider, C. M. High resolution electron energy loss spectroscopy of spin waves in ultra-thin cobalt films. *Surf. Interface Anal.* **2016**, *48*, 1104-1107.

Figure Captions:

Figure 1. A schematic in TEM visualization of colloidal nanocrystal growth and electrochemical liquid reactions.

Figure 2. (A) A schematic shows the atomic growth of a nanoparticle. (B) The atomic growth of the (110) facet of a platinum nanoparticle. The red dots show the newly added Pt atoms. (C) The schematic shows the self-assembly of nanoparticles. (D) The observed self-assembly for PbSe nanoparticles in a liquid cell. (E) Comparison of different growth trajectories of platinum nanoparticles. Enlarged (1.5 times) color images from an in situ movie showing simple growth by monomer addition (left column) or growth by coalescence between nanoparticles (right column). Distinct contrast changes are highlighted with arrows indicating recrystallization within the particle after coalescence. see ref.[2] and Movie S1. More details about (B and C) can be found in ref.[49]; see Movie S2.

Figure 3. (A) A schematic illustrating the growth of a nanocube in a liquid solution. (B) Sequential images show the growth of a Pt nanocube [49]. (C) A schematic showing nanowire formation by shape-directed nanoparticle attachment. (D) Sequential TEM images showing the growth of a Pt_3Fe nanorod[16]. Time is displayed as minutes: seconds. Initial time is arbitrary. Nanorods and the specific particles as building blocks for nanorod formation are highlighted in green. see Movie S3. (E) A schematic demonstrating the stereo-hindrance effects during growth. (F) Sequential images indicate the growth of platinum iron nanocrystals in a solvent with 50% oleylamine[25]. Nanoparticles are highlighted in green. see Movie S4.

Figure 4. (A) Dynamics of nanoparticles aligned in one-dimensional chains. Chains formed at the beginning of assembly have a particle connectivity that is tracked over time to illustrate folding and clumping behavior. (B) Energy and stability of self-assembly. Colored circles indicate location of nanoparticles overlaid on original image. White arrows indicate dipole orientations. The color corresponds to the total energy of an individual nanoparticle computed from the dipole and van der Waal interaction with nearby particles. (C) Identification of a nanoparticle by image processing. (D) A schematic and the TEM image of the CoO nanoparticles assembled around a nanodroplet of growth solution[28]. Note: the original figures about (A-C) are from ref.[17]

Figure 5. (A) An illustration of spinel ferrite M-Fe oxide growth in liquid cell TEM. (B) An illustration of Fe oxide growth in a liquid cell. (C) Sequential images captured during growth of Fe_3Pt-Fe_2O_3 core-shell nanostructures. see Movie S5. (D) EDS mapping of one core-shell nanoparticle. Blue represents Pt, and orange is for Fe. (E) A schematic

summarizes the formation pathway of Fe_3Pt-Fe_2O_3 core-shell hetero-structure. see ref.[35]

Figure 6. (A) Time series of TEM images showing growth and dissolution of Pb dendrites. See Ref.[50] and Movie S6. (B) A cartoon showing the electrochemical growth of lead dendrites. (C) Time evolution of the growth and dissolution of lithium dendrite. See Ref.[49] and Movie S7.

Figure 7. (A) Time series of TEM images show the morphological evolution of MoS_2 nanosheets on the Ti electrode with $LiPF_6$/EC/DEC electrolyte in a liquid cell. (B) I. A schematic showing nano-beam diffraction characterization of SEI layer or residual MoS_2 products after the reaction. II. Long camera length (770 mm) STEM image with nano-beam diffraction series acquired in the marked red dash box area. (C) Evolution of Au electrode when electrochemically reacted with lithium electrolyte. Expansion and cracking are observed. (D) Time series of TEM images showing the fragmentation of Au electrode during Li-Au reaction. During this explosive reaction, a large number of nanoparticles splashed from Au electrode to the surrounding area of the electrode. (E) Time evolution of the dissolution of Au electrode in $LiPF_6$/EC/DEC electrolyte. Note: the original figures of (A-B) are from Ref.[53]; see Movie S8. (C-E) can be found in Ref.[65].

Figure 8. (A) I. Time series of TEM images showing the growth of a gas bubble emerged between the gold electrode and the SEI film. see Ref.[49] and Movie S9. II. HAADF image of the SEI layer on Ti electrode with the highlighted red dash box indicating nano-beam diffraction acquiring area. III. Reconstructed bright field image obtained from the diffraction series. IV. Reconstructed virtual diffraction patterns selected from regions marked "IV" in panel III. V. Virtual dark-field image reconstructed using the selected single diffraction spot in panel IV. see Ref.[65] (B) Gas bubbles formation during lithiation of Au electrode. (C) Sequential images showing the bubbles at the electrode-electrolyte interfaces on both sides of electrodes in two electrodes electrochemical cells.[53]

Figure 9. A powerful liquid cell TEM platform built upon the liquid cell development, advanced imaging, fast electron detection, computational design and data analysis (Some image components curtesy of Emory Chan, Peter Ercius and Lin-Wang Wang).

Figure 1

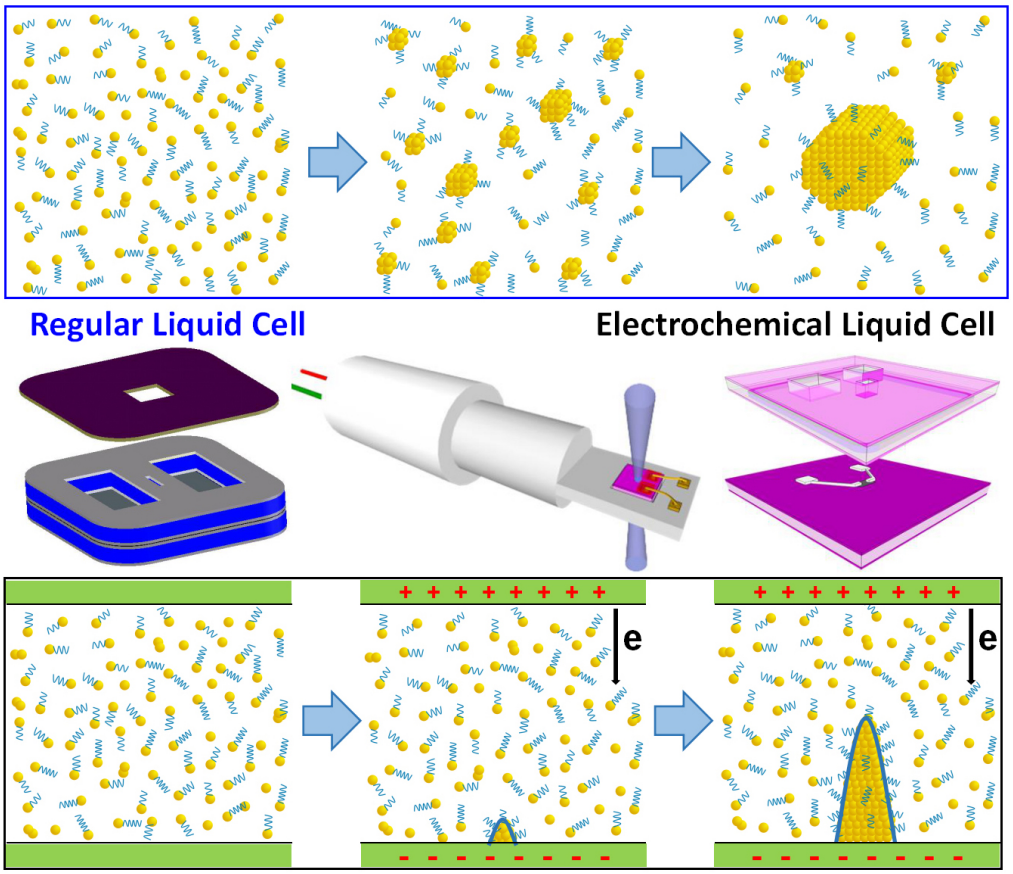

Figure 2

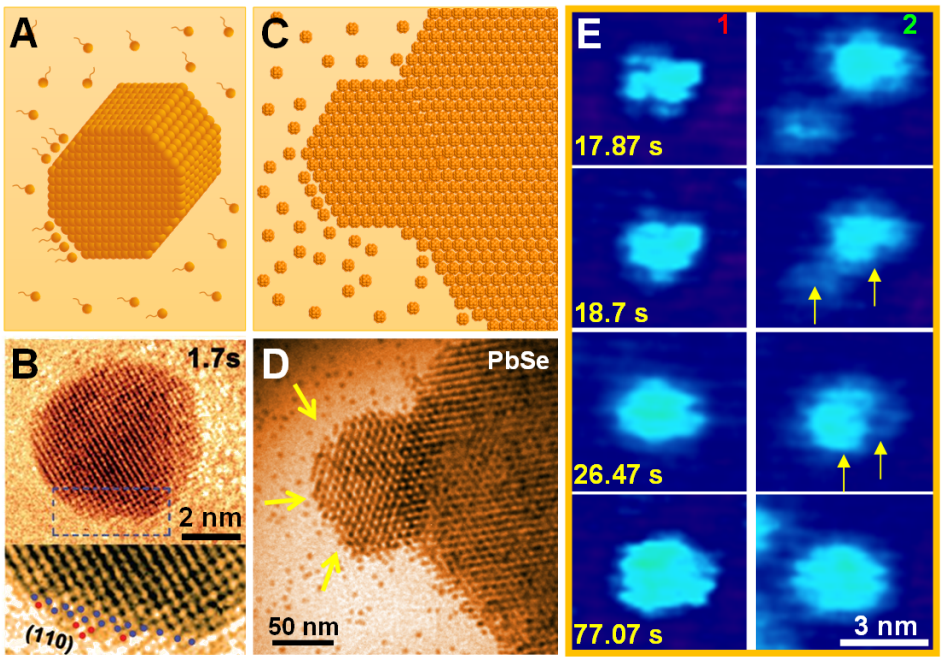

Figure 3

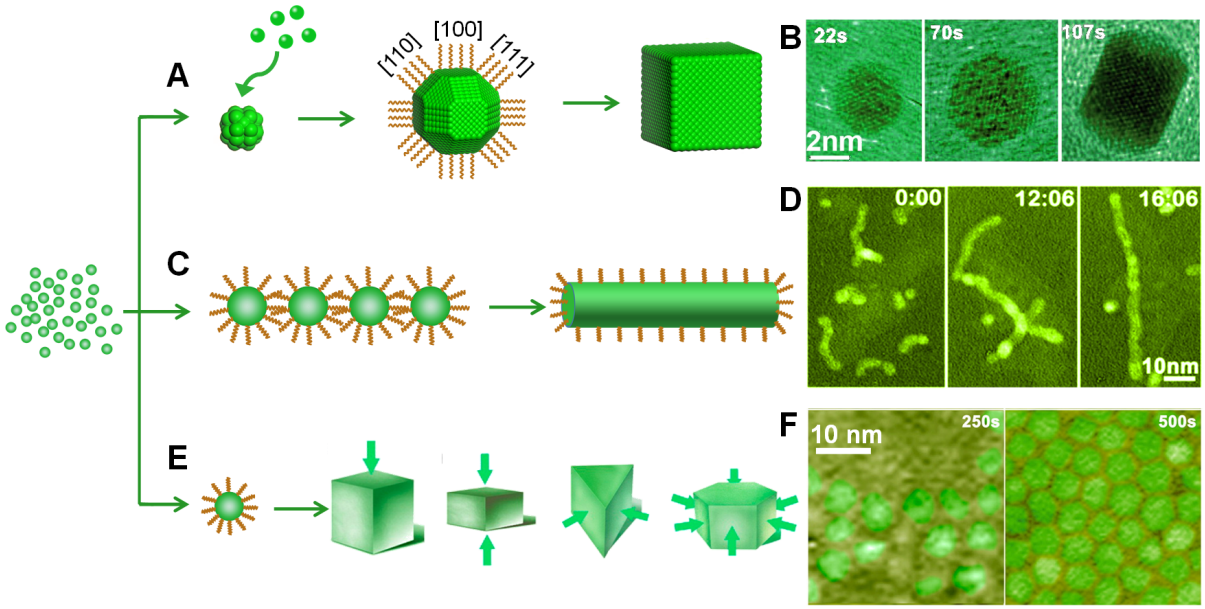
A
[110]
[100]
[111]
B
22s
70s
107s
2nm
C
D
0:00
12:06
16:06
10nm
E
F
10 nm
250s
500s

Figure 4

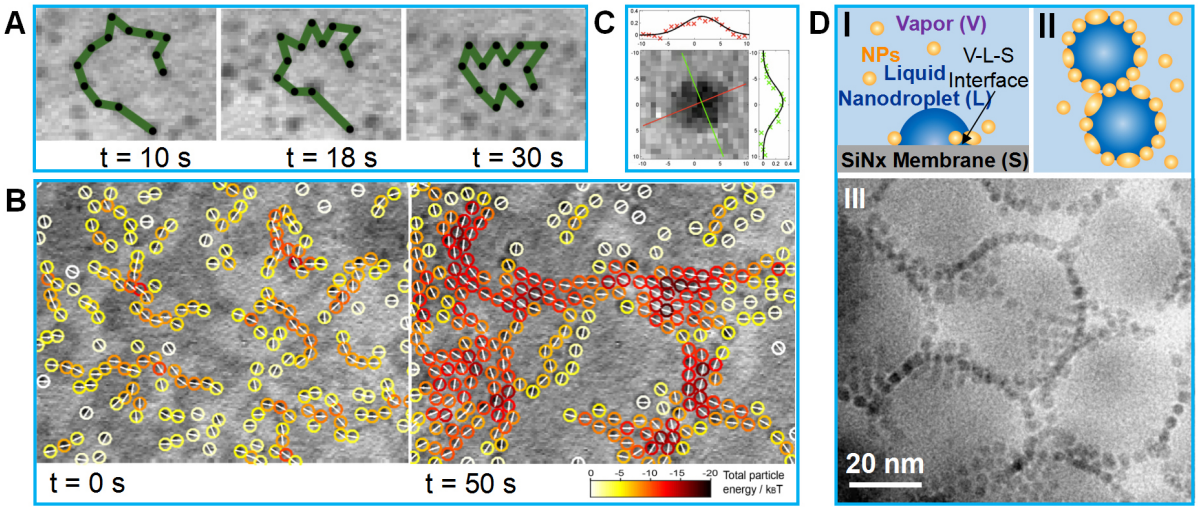
A
t = 10 s
t = 18 s
t = 30 s
B
t = 0 s
t = 50 s
0 -5 -10 -15 -20 Total particle energy / kBT
C
D
I
Vapor (V)
NPs
Liquid
V-L-S Interface
Nanodroplet (L)
SiNx Membrane (S)
II
III
20 nm

Figure 5

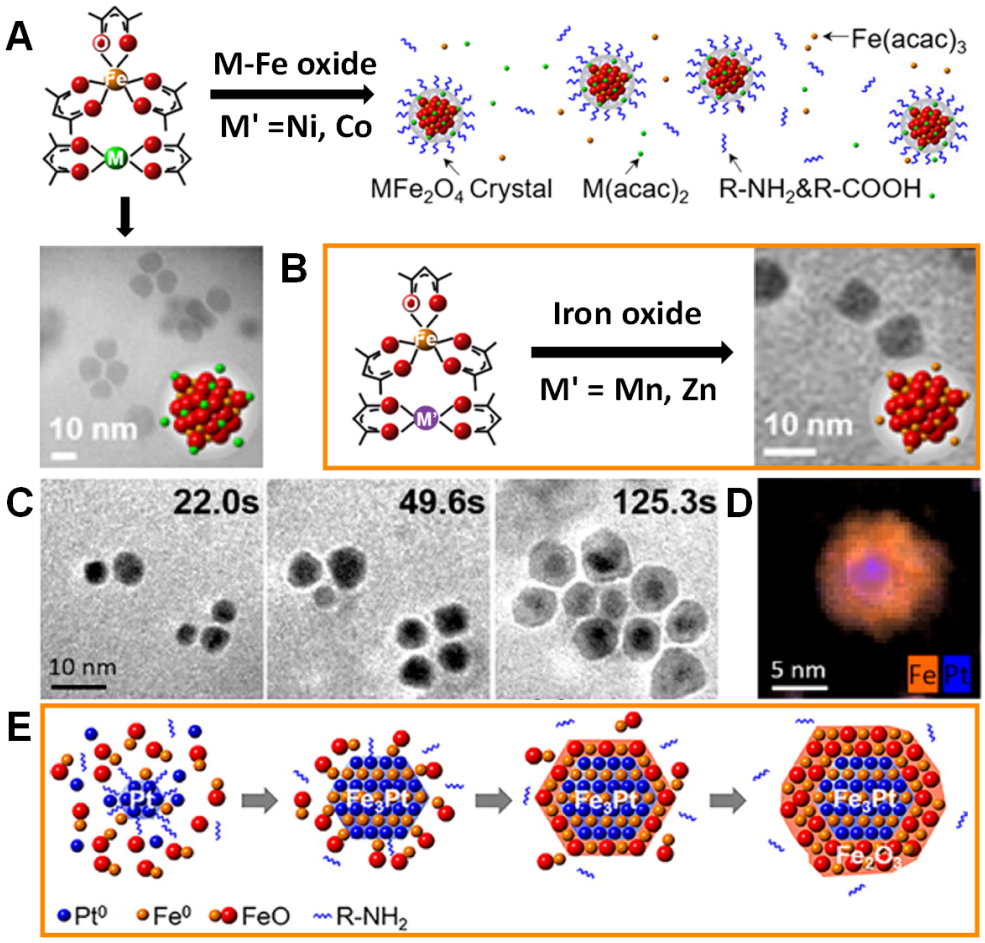
A
M-Fe oxide
M' =Ni, Co
Fe(acac)3
MFe2O4 Crystal
M(acac)2
R-NH2&R-COOH
10 nm
B
Iron oxide
M' = Mn, Zn
10 nm
C
22.0s
49.6s
125.3s
10 nm
D
5 nm
Fe
Pt
E
Pt0
Fe0
FeO
R-NH2

Figure 6

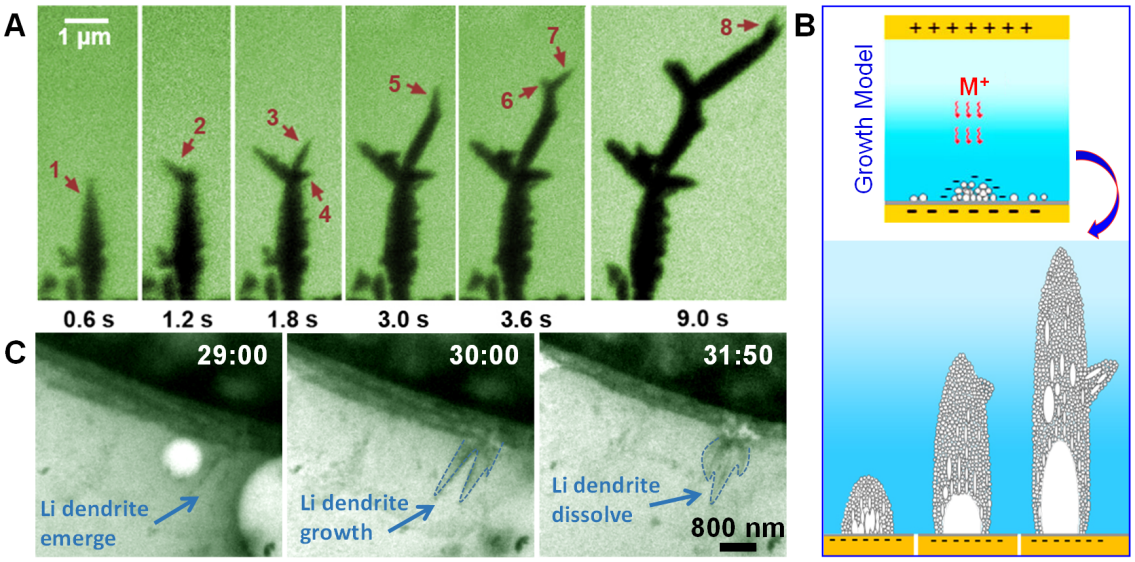
A
1 μm
1
2
3
4
5
6
7
8
0.6 s
1.2 s
1.8 s
3.0 s
3.6 s
9.0 s
B
Growth Model
M+
C
29:00
30:00
31:50
Li dendrite emerge
Li dendrite growth
Li dendrite dissolve
800 nm

Figure 7

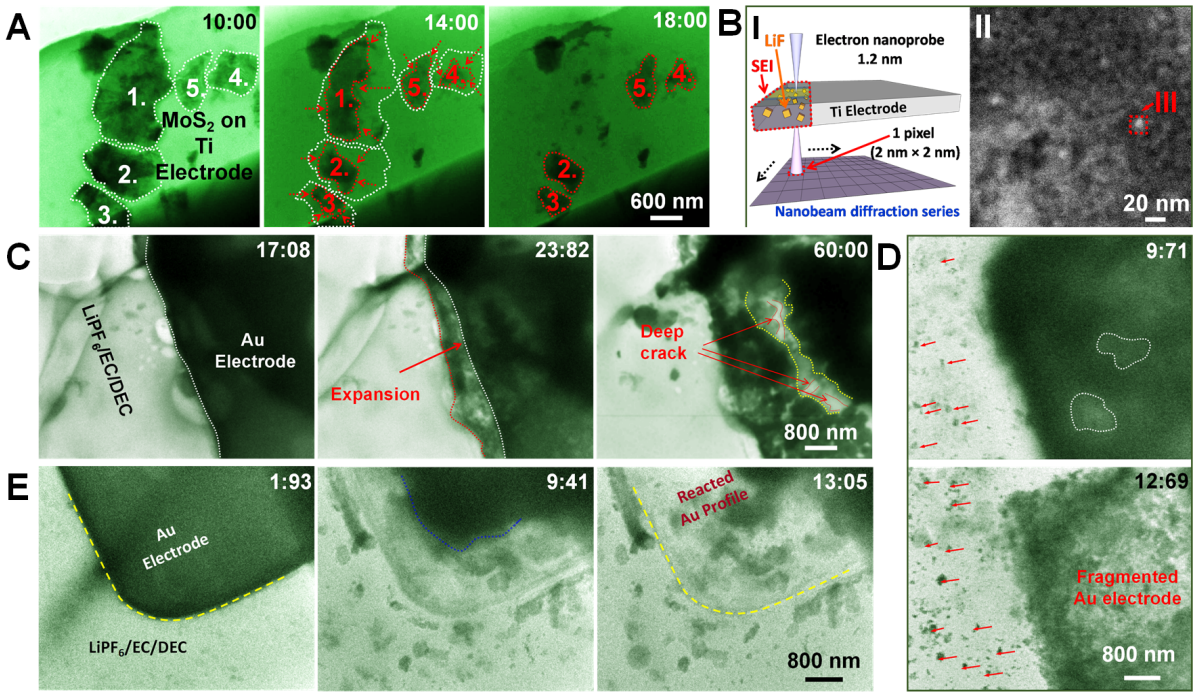
A
10:00
14:00
18:00
1.
2.
3.
4.
5.
MoS2 on Ti Electrode
600 nm
B
I
LiF
SEI
Electron nanoprobe
1.2 nm
Ti Electrode
1 pixel
(2 nm × 2 nm)
Nanobeam diffraction series
II
III
20 nm
C
17:08
23:82
60:00
LiPF6/EC/DEC
Au Electrode
Expansion
Deep crack
800 nm
D
9:71
12:69
Fragmented Au electrode
800 nm
E
1:93
9:41
13:05
Au Electrode
LiPF6/EC/DEC
Reacted Au Profile
800 nm

Figure 8

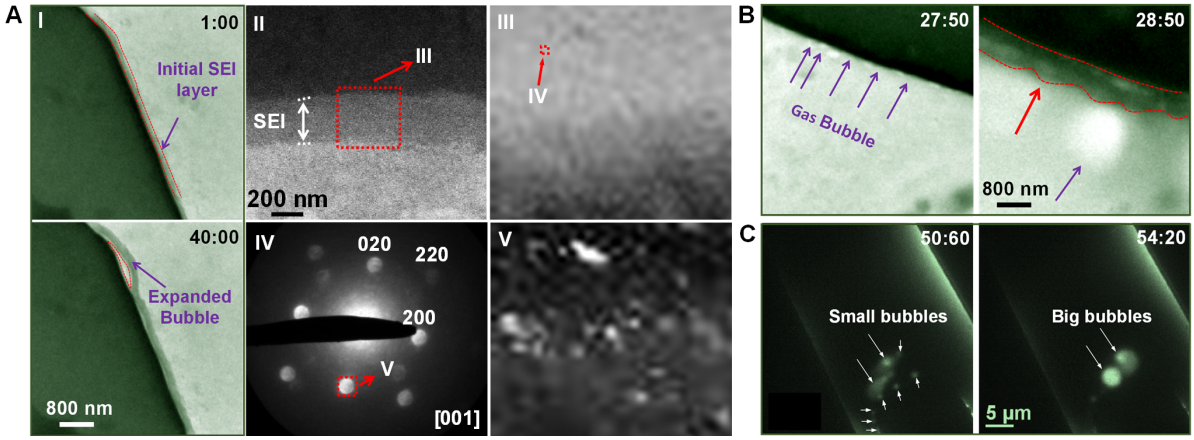
A
I
1:00
Initial SEI layer
40:00
Expanded Bubble
800 nm
II
III
SEI
200 nm
IV
020
220
200
V
[001]
III
IV
V
B
27:50
Gas Bubble
28:50
800 nm
C
50:60
Small bubbles
54:20
Big bubbles
5 μm

Figure 9

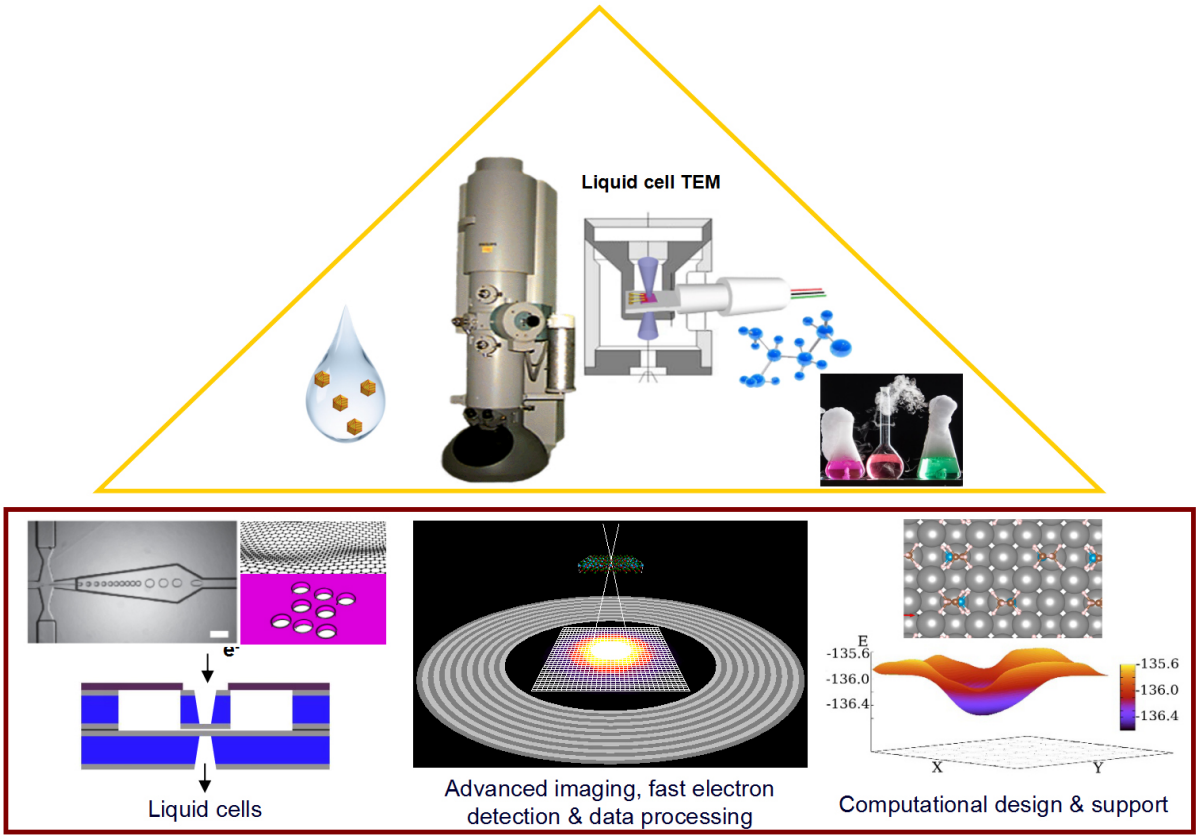
Liquid cell TEM
e-
Liquid cells
Advanced imaging, fast electron detection & data processing
E
-135.6
-136.0
-136.4
X
Y
Computational design & support